Structural, magnetic, and dielectric properties of W/Cr co-substituted Aurivillius $Bi_5FeTi_3O_{15}$

Xuzhong Zuo [a, *], Maolian Zhang [a], Enjie He [a], Banggui Guan [a], Yanfu Qin [a], Jie Yang [b], Xuebin Zhu [b], Jianming Dai [b]

[a] College of Electrical and Electronic Engineering, Anhui Science and Technology University, Fengyang 233100, People's Republic of China
[b] Key Laboratory of Materials Physics, Institute of Solid State Physics, Chinese Academy of Sciences, Hefei 230031, People's Republic of China

ABSTRACT

We investigate the structural, magnetic, and dielectric properties of Aurivillius $Bi_5FeTi_{3-3x}(WCr_2)_xO_{15}$ ($0 \leq x \leq 0.15$) multiferroic ceramics. All the samples can be determined to be an orthorhombic structure and space group of $A2_1am$. The magnetic measurements reveal that the short-range antiferromagnetic exchange interaction can be strengthened by doping Cr^{3+} ions at Ti sites. The ferroelectric Curie temperature T_c decreases from 1013 K to 965 K. One dielectric relaxation dates from the long-range motion of oxygen vacancies can be observed in all the samples. However, the doped samples exhibit another one dielectric relaxation, which is relate to the localized hopping process of electrons. In addition, the *dc* conduction behavior in all the samples can be attributed to the long-range motion of oxygen vacancies.

© 2017 Elsevier B.V. All rights reserved.

1. Introduction

The bismuth-based Aurivillius phase materials exhibit the co-existence of magnetic, ferroelectric (FE) or ferroelastic order, have attracted much attention because of their potential device application in magnetic sensors, data storage, and digital memories, etc. [1−3] The general formula of Aurivillius compound is $(Bi_2O_2)^{2+}(A_{n-1}B_nO_{3n+1})^{2-}$ (A = Na, Sr, Bi, etc., B═Ti, Fe, etc.), and the perovskite layers $(A_{n-1}B_nO_{3n+1})^{2-}$ is interlayered between the fluorite-like layers $(Bi_2O_2)^{2+}$, and n refers to the layer number of the perovskite-like layers [4,5].

The previous studies on Aurivillius phase compounds are focus on the ferroelectric and dielectric properties of Bi_3TiNbO_9 ($n = 2$) and $Bi_4Ti_3O_{12}$ (BTO, $n = 3$) because these materials is lack of long-range magnetic ordering [6−8]. However, a typical four-layered $Bi_5FeTi_3O_{15}$ (BFTO) can be obtained by inserting 1 mol $BiFeO_3$ into 1 mol BTO, and the magnetic behavior of BFTO has been determined to be AFM ordering [9]. Meaningful, Mao found that the magnetic behavior can be modified from AFM to FM state by introducing a half amount of Co ions at Fe sites in BFTO [10]. Later, the regulation of magnetic behavior was investigated widely by

doping magnetic ions Fe, Cr, Mn, and Ni at Fe or Ti sites in Aurivillius compounds with different perovskite layer number n, and the observed intrinsic FM can be attributed to the spin canting of oxygen octahedron [11−15]. *Yuan* reported that doping Co ions for Ti ions in $Bi_6Fe_2Ti_3O_{18}$ can effectively improve the FM Curie temperature compared with doping Co ions for Fe ions [16], which imply doping magnetic ions at Ti sites may be an effective routine to optimize the magnetic behavior of Aurivillius phase.

It is well known that the existence of oxygen vacancies in Aurivillius oxides due to the escape of oxygen from the lattice in high-temperature sintering process is an irrefutable fact. Moreover, the factor of oxygen vacancies in ferrolectrics is suggested to be critical in determining the dielectric and electric performance [17−19]. For example, the thermal movement and aggregate effect of oxygen vacancies may increase electric conduction and block the ferroelectric domain switching, respectively [20]. Some literature have reported that substituting tiny amount of high valence state donor ions in Aurivillius oxides can effectively suppress the formation of oxygen vacancies and thus improve the electric properties [21,22]. Certainly, analyzing the evolution rule of the dielectric and electric properties by doping donor ions will be essential and beneficial for further explore and design the high-performance single-phase multiferroics in Aurivillius phase. Up to now, the previous studies on displace effects of donor ions on dielectric and electric properties are mainly focus on the ferroelectric-based

---

Aurivillius compounds with $n = 2$ and $n = 3$ [23,24]. However, the detailed investigations on the effects of high valence state ions substitution on structural, dielectric and electric properties of multi-based Aurivillius $Bi_5FeTi_3O_{15}$ ($n = 4$) are still lacking.

Based on the above discussion, we selected donor ions W^{6+} and magnetic ions Cr^{3+} as doping elements, and systemically investigated the structural, magnetic, dielectric and electric properties of W/Cr co-doped Aurivillius $Bi_5FeTi_{3-3x}(WCr_2)_xO_{15}$ ($0 \leq x \leq 0.15$) by the measurements of x-ray diffraction, microstructure, magnetization, dielectric response, impedance spectroscopy, electric modulus spectroscopy, ac conductivity, and scaling behaviors.

2. Experimental procedure

The polycrystalline ceramics $Bi_5FeTi_{3-3x}(WCr_2)_xO_{15}$ ($0 \leq x \leq 0.15$) were prepared by the conventional solid state reaction method. Firstly, the stoichiometric amounts of high purity Bi_2O_3 (99.975%, 10 wt% excess Bi_2O_3 to compensate volatilization of Bi during the high-temperature sintering procedure), Fe_2O_3 (99.99%), Ti_2O_3 (99.9%), WO_3 (99%), and Cr_2O_3 (99.99%) were mixed and ground and then calcined at 600 °C for 20 h. Secondly, the calcined powders were ground, pelletized, and sintered at 850 °C for 10 h with an intermediate grinding, and finally the furnace was cooled slowly to room temperature (RT). The crystal structure was determined with powder XRD (Philips X'Pert PRO) using Cu $K\alpha$ radiation at RT. A field-emission scanning electron microscope (FE-SEM, Sirion 200, FEI Company) was used to characterize the surface morphology of the samples. The magnetic measurements were carried out with a quantum design superconducting quantum interference device (SQUID) magnetic property measurement system (MPMS) system ($2 \leq T \leq 400$ K, $0 \leq H \leq 5$T) (PPMS-9, Quantum Design, CA, USA). The temperature dependence of dielectric responses were measured with an LCR meter (TH2828S) in the frequency and temperature range of 1 kHz–1MHz and 300–1050 K, respectively. The frequency dependence of complex impedance spectroscopy and electric modulus spectroscopy were measured with an LCR meter (TH2828S) in the frequency 20 Hz–1 MHz at various temperatures ranging from 400 to 700 K.

3. Results and discussion

Fig. 1(a) shows the XRD patterns of all samples at RT, and we can note that all samples are single phase without the detectable impurities. Meanwhile, we refined the structural information using the program Rietica and the fitted results of a typical sample with $x = 0.15$ are given in Fig. 1(b). Moreover, all samples can be indexed with layer-structured perovskite Aurivillius phase with the space group of $A2_1am$, which is consistent with the previously reported results [25]. The evolution of lattice parameters with x is shown in Fig. 1(c). We can found that both lattice parameters a and b decrease slightly whereas c and cell volume V increase apparently upon increasing x. Take into account of the content of Cr element is two times as much as that of W element and the ionic radius of Cr^{3+}, W^{6+}, and Ti^{4+} is 0.615 Å, 0.60 Å, and 0.61 Å respectively. Therefore, the increase in V can be mainly attributed to the introduction of Cr ions, which is in line with the shift of enlarged main diffraction peak (119) towards a lower angle (not shown here). It can be seen from Fig. 1(a) that the intensity of the diffraction peaks (006) and (008) gradually decreases while that of peak (200)/(020) increases with increasing the doping level x, implying that the substitution of W/Cr may promote the $a(b)$- axis orientation growth of grain. In Aurivillius phase, the orthorhombicity is the factor that is usually used to evaluate the lattice distortion. Hence, we calculated the orthorhombicity of crystal structure according to the formula of $2(a-b)/(a+b)$, and it can be determined to be 0.00510,

0.00483, 0.00465, and 0.00472 for the sample with $x = 0$, 0.05, 0.1, and 0.15, respectively, which indicate the lattice distortion decreases with increasing the doping level. The evaluation of lattice distortion can be attributed to the W^{6+} possess a higher $5d^0$ configuration compared with $3d^0$ of Ti^{4+} [24]. Fig. 2 shows the SEM images of all the samples, SEM results show all the samples have a relatively uniform and dense microstructure with the plate-like grain. In general, the substitution of Cr ions in Aurivillius phase can promote the grain's growth, and the grain becomes more larger and thicker [12]. However, the doping of W ions may influence the grain kinetics because it can suppress the grain boundary diffusion in the sintering process, which can lead to a better arrangement of particles and consequently to an improved compactness [26]. As a result, the substitution of W/Cr can further increase the grain size and improve the densification of ceramics.

In order to investigate the influence of W/Cr co-doping on the magnetic properties, we measured the temperature dependence of magnetization of all samples from 5 K to 300 K, as shown in Fig. 3. The magnetization (M) versus temperature (T) plots of all the samples were measured at H = 100Oe in the zero-field-cooled (ZFC) and field-cooled (FC) modes. The monotonous increase in the magnetization with decreasing temperature implies that all the samples exhibit a paramagnetic- or antiferromagneteic-like behavior. Moreover, the quantitative evaluation of M-T data in FC
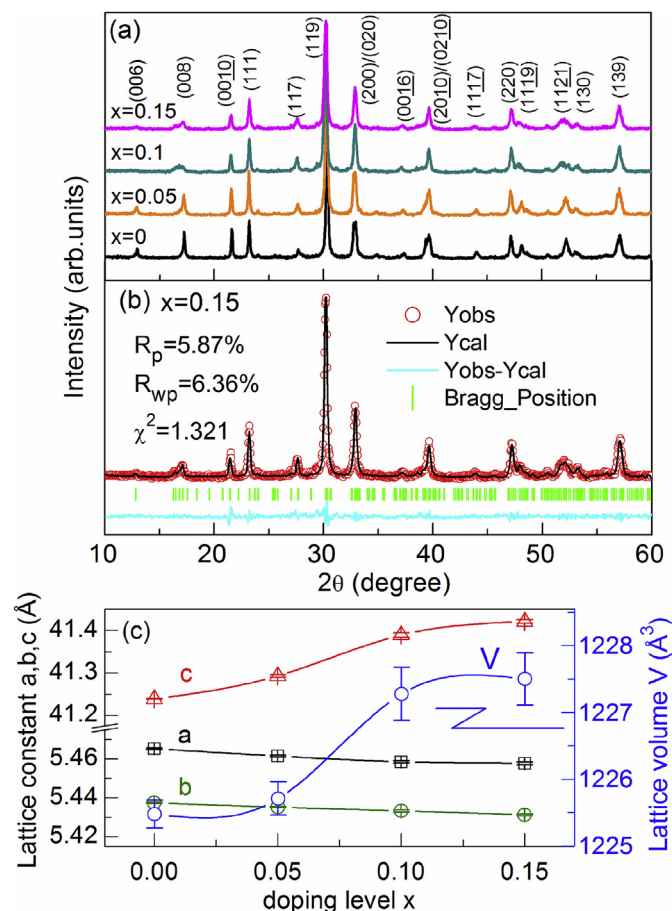

Fig. 1. (a) XRD patterns of $Bi_5FeTi_{3-3x}(WCr_2)_xO_{15}$ ($0 \leq x \leq 0.15$). (b) XRD patterns of the $x = 0.15$ sample. Circles indicate the experimental patterns, and the calculated patterns are the continuous line overlapping them. The lowest curve shows the difference between the experimental and calculated patterns. The vertical bars indicate the expected reflection positions. (c) Lattice parameters a, b, c, and V as a function of the doping level x.
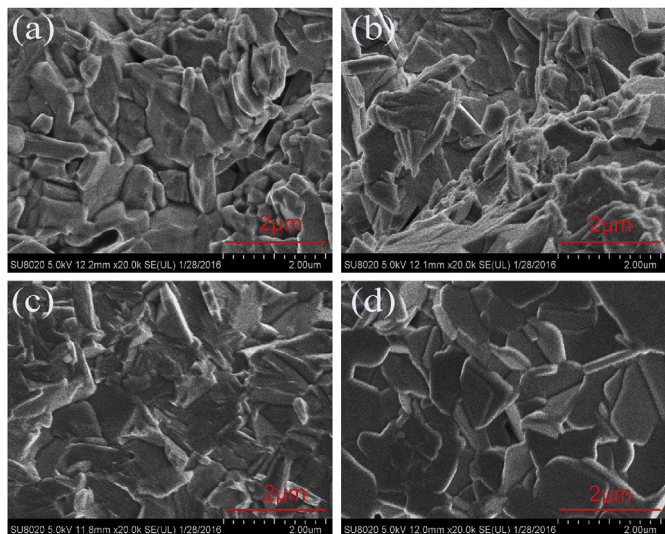
Fig. 2. The representative FM-SEM images of $Bi_5FeTi_{3-3x}(WCr_2)_xO_{15}$ with (a) $x = 0$, (b) $x = 0.05$, (c) $x = 0.1$, and (d) $x = 0.15$.

mode is fitted by the modified Curie-Weiss relation: $M(T,H)/H = \chi_0 + C/(T - \theta)$, where the first term χ_0 is the temperature-independent susceptibility, the later term $C/(T-\theta)$ is the Curie-Weiss susceptibility, θ is the Curie-Weiss temperature, and C is the Curie constant [12]. The fitted results manifest that the experimental data can be well described by the Curie-Weiss relation, as shown in Fig. 3. In addition, the very small values of χ_0 [the left panel of Fig. 4(e)] reflect a rather weak non-paramagnetic contribution. Furthermore, the fitted values of θ for all the samples are negative, implying all the samples are the nature of antiferromagnetic (AFM) interaction, as shown in the right part of Fig. 4(e). Meanwhile, the value of θ decreases with increasing x illustrating AFM interaction is improved, as evidenced by the nonlinear behavior of inverse magnetic susceptibility $1/\chi = H/M$ becoming more and more obvious in low-temperature region with increasing x, as shown in the right panel of Fig. 3. In addition, we

calculated the effective magnetic moment u_{eff} according to $C = Nu^2_{eff}/3k_B$ and found u_{eff} monotonously decreases from 3.22 to $2.82\mu_B$ for the sample from $x = 0$ to $x = 0.15$, as displayed in the left panel of Fig. 4(f), which can further confirm the AFM interaction can be heightened by doping W/Cr.

In order to further make clear the detailed magnetic structure, the magnetic field dependence of magnetization M-H plots were performed at 300 K and 5 K, as shown in Fig. 4(a) and (b), respectively. All the M-H plots at 300 K show a notable linear behavior and do not saturate even magnetic field up to 4.5T, indicating all the samples are nature of AFM interaction. However, the M-H plots at 5 K manifest a different behavior compared to that at 300 K. A small loop can be observed under low magnetic field range, as shown in Fig. 4(d), implying a weak and short-range FM state exists in the samples. On one hand, W^{6+}/Cr^{3+} ions have a different ionic radius compared with that of Ti^{4+}, which may induce the distortion of crystal structure and give rise to the canted spin structure of the tilted $Fe(Cr)O_6$ [27]. On the other hand, the valence state transfer of tiny amount of Fe and Cr may introduce the presence of Fe^{3+}-O-Fe^{2+} and Cr^{3+}-O-Cr^{2+} ferromagnetic exchange interaction [28]. These two factors may account for the observation of a weak FM behavior in the samples. Actually, both the distorted crystal structure leads to the spin canting in perovskite-based oxides and the valence state transfer of magnetic ions brings about the FM interaction in Aurivillius phase have been reported [26–28]. And also, the saturated magnetization M_s can be obtained according to the fitting results [shown in Fig. 4(c)] of the Brillouin function [29,30].

$$M = M_S\left\{\left(\frac{2J+1}{2J}\right)\coth\left[\frac{(2J+1)y}{2J}\right] - \left(\frac{1}{2J}\right)\coth\left(\frac{y}{2J}\right)\right\}$$

where $y = g\mu_BJH/k_B(T + T_0)$, M_s is the saturation magnetization, μ_B is the Bohr magneton, g is the spectroscopy splitting factor, J denotes an average value assumed to represent the mole ratio of high-spin of Fe^{3+} and Cr^{3+}, and T_0 represents a measure of the interaction preventing the complete alignment of Fe and Cr spins even at the highest field. The fitted results show the M_s decreases gradually from 3.72 *emu/g* to 3.06 *emu/g* with increasing the doping level from $x = 0$ to 0.15, as shown in Fig. 4(f). The decrease in the M_s is
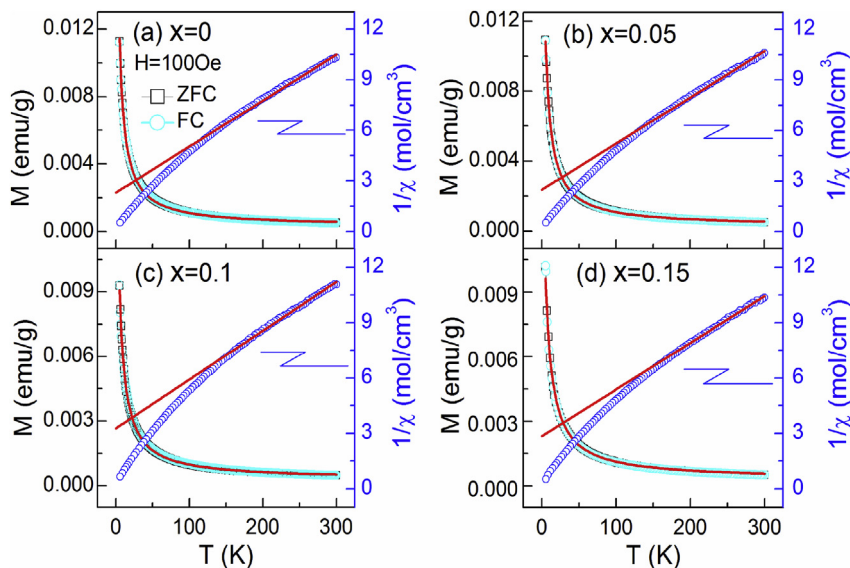

Fig. 3. The temperature dependence of magnetization in ZFC and FC modes measured at H = 100Oe, the relevant inverse magnetic susceptibility $(1/\chi)$ versus temperature (T) in FC mode, and the fitted curves (Red line) in the PM range according to the Curie-Weiss Law for the sample $Bi_5FeTi_{3-3x}(WCr_2)_xO_{15}$ with (a) $x = 0$, (b) $x = 0.05$, (c) $x = 0.1$, (d) $x = 0.15$. (For interpretation of the references to colour in this figure legend, the reader is referred to the web version of this article.)
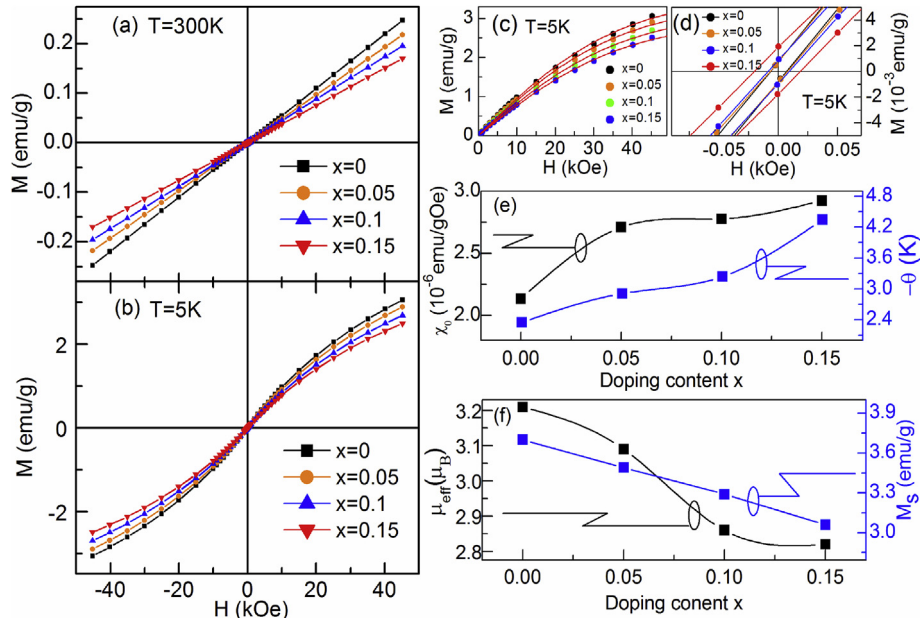
Fig. 4. Magnetic field dependence of the magnetization for all the samples measured at (a) 300 K and (b) 5 K. (c) The fitted plots of magnetic field-dependent magnetization at 5 K according to the modified Brillouin function. (d) The enlarged magnetization plots under low magnetic field region. (e) The fitted non-paramagnetic susceptibility χ_0 and Curie Weiss temperature θ according to the Curie-Weiss relation. (f) Evaluation of the calculated effective magnetic moment u_{eff} and the fitted saturated magnetization M_s for all the samples.

well satisfied with the evaluation result of u_{eff}, as shown in Fig. 4(f). Based on the above results, we can note that both Curie temperature θ, the effective magnetic moment u_{eff}, and the saturated magnetization M_s exhibit the decrease behavior with increasing x, which can together prove that the AFM interaction in the samples is strengthened caused by W/Cr co-doping. The similar experimental conclusion has been found in Nb and more Fe ions co-doped Aurivillius materials [31].

The temperature dependence of dielectric constant ε' and dielectric loss $\tan\delta$ range from 300 to 1050 K at different frequencies are shown in Figs. 5 and 6, respectively. For all the samples, one can note that ε' first increases slowly; and then, it shows an obvious dielectric anomaly behavior; and later, it exhibits an abrupt increase. Interestingly, the dielectric anomaly behavior shifts to a lower temperature region and the dispersion behavior becomes more and more remarkable with increasing doping level x, as shown in Fig. 5. For instance, the dielectric anomaly behavior of the sample $x = 0$ and $x = 0.15$ located at the temperature region of 500—800 K and 350—700 K, respectively. In general, the dielectric anomaly is usually related to the thermal movement of charge carriers and the dielectric anomaly in different temperature region may be related to the different charge carrier motion [32,33]. Meanwhile, the ferroelectric Curie point T_c can be determined to be 1013, 1007, 981, and 976 K for the sample $x = 0$, 0.05, 0.1, and 0.15, respectively. The decrease in T_c with increasing x may be ascribed to the suppressed lattice distortion. The dielectric loss for all the samples show a similar behavior, i.e., $\tan\delta$ first increases slowly between 300 and 600 K and then increases abruptly above 600 K. It should be noted that the dielectric loss relaxation in 300—570 K can be only observed in the sample with $x = 0.1$ and 0.15, as shown in the inset of Fig. 6(c) and (d), respectively. The relationship between the dielectric relaxation temperature and frequency can be well fitted by Arrhenius Law $f_r = f_0 \exp(-E_a/k_B T)$. As a result, the activation energy E_a can be obtained as 0.32 eV and 0.33 eV for the sample $x = 0$ and $x = 0.15$, respectively, as shown in Fig. 6(e). The origination of dielectric loss relaxation in this temperature region

may be arising from the hopping process of electrons [34], which will be further discussed by both the frequency-dependent complex dielectric response and electric modulus M'' plots, as shown below.

The dielectric anomaly behavior has been observed in the temperature-dependent dielectric constant spectroscopy, as shown in Fig. 5. Meanwhile, the dielectric loss relaxation in 300—500 K has been found in sample $x = 0.1$ and 0.15, as shown in Fig. 6. Hence, we performed the frequency dependence of dielectric constant and loss in the temperature range of 400 K—700 K for all the samples to ascertain the mechanism of relaxation [35]. As a result, the frequency-dependent dielectric constant and loss spectroscopy
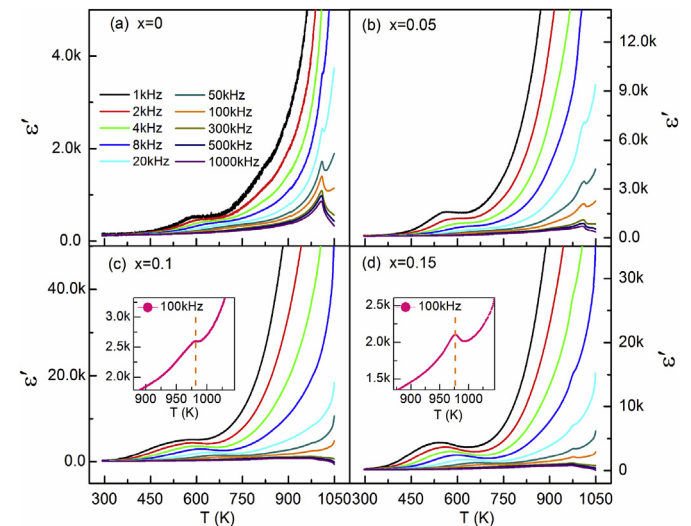

Fig. 5. Temperature dependence of the dielectric constant at the frequency of 1, 2, 4, 8, 20, 50, 100, 300, 500, and 1000 kHz for $Bi_5FeTi_{3-3x}(WCr_2)_xO_{15}$ with (a) $x = 0$, (b) $x = 0.05$, (c) $x = 0.1$, and (d) $x = 0.15$. The inset of (c) and (d) shows the enlarged dielectric constant in the temperature range of 875 K—1040 K at 100 kHz for the sample with $x = 0.1$ and $x = 0.15$, respectively.
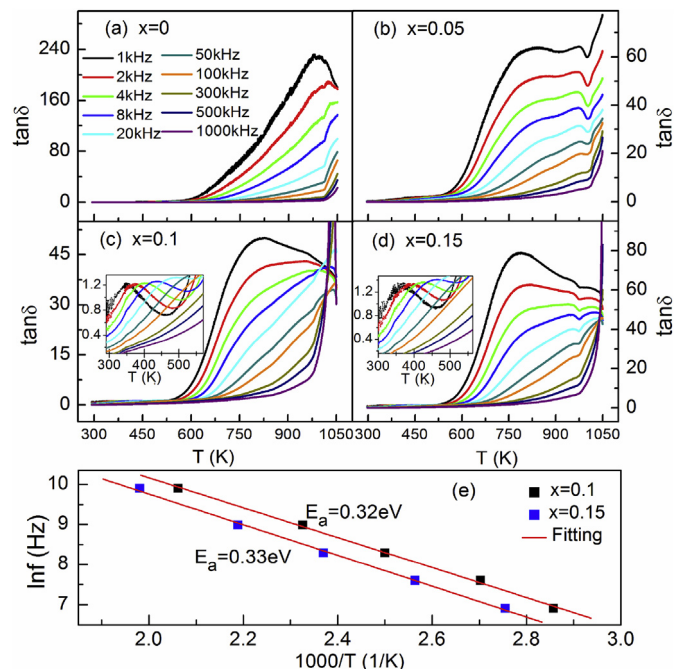
Fig. 6. Temperature dependence of the dielectric loss at the frequency of 1, 2, 4, 8, 20, 50, 100, 300, 500, and 1000 kHz for $Bi_5FeTi_{3-3x}(WCr_2)_xO_{15}$ with (a) $x = 0$, (b) $x = 0.05$, (c) $x = 0.1$, and (d) $x = 0.15$. The inset of (c) and (d) shows the magnified dielectric loss in the temperature range of 300–570 K for the sample with $x = 0.1$ and $x = 0.15$, respectively. (e) Arrhenius plots for relaxation frequency versus temperature for the sample with $x = 0.1$ and $x = 0.15$.

indicate the dielectric relaxation behavior can be also only found in the samples with $x = 0.1$ and $x = 0.15$. For simplicity, we take the sample $x = 0.1$ as an example to analyze the frequency-dependent dielectric constant and dielectric loss information, as shown in Fig. 7(a) and (b). One can note that the dielectric constant shows an obvious relaxation behavior, as shown in the inset of Fig. 7(a). And also, two dielectric relaxations can be clearly found in dielectric loss plots, as marked by the dotted lines and shown in Fig. 7(b). The relationship between the relaxation characteristic peak and the temperature in high frequency region can be well described by the Arrhenius Law $f_r = f_0\exp(-E_a/k_BT)$. Thus, the activation energy E_a can be determined to be 0.31 eV, as shown in inset of Fig. 7(b). The activation energy for the sample $x = 0.15$ is 0.32 eV (not shown here).

In addition, it is well known that the modulus M'' spectroscopy is an effective way to check the dielectric relaxation information in the absence of the dielectric relaxation peak [36,37]. Hence, we calculated the modulus imaginary part M'' spectroscopy according to the formula $M'' = \varepsilon''/(\varepsilon'^2 + \varepsilon''^2)$ for all the samples. We also take the sample $x = 0.1$ as an example and the frequency dependence of M'' spectroscopy for the sample $x = 0.1$ is displayed in Fig. 7(c). We can find that the peak of M'' are almost located at high frequency region and the peaks shift to a higher frequency with increasing the temperature, which is a typical feature of dielectric relaxation [38]. The similar behavior can be observed for all the samples (not shown here). The relationship between the peak position and temperature can be also fitted by the Arrhenius Law $f_r = f_0\exp(-E_a/k_BT)$, and the activation energy from M'' spectroscopy can be determined to be 0.67 eV, 0.50 eV, 0.31 eV, and 0.31 eV for the sample with $x = 0$, 0.05, 0.1, and 0.15, respectively, as given in Fig. 7(e). We can note that the activation energy deduced from the electric modulus M'' decreases from 0.67 eV to 0.31 eV with increasing x, implying the mechanism of dielectric relaxation varies

with the doping level x.

The dielectric relaxation may arising from the thermal movement of charge carriers, which can also induce the electric conduction behavior [34]. The imaginary part Z'' of impedance spectroscopy can provide the conductive information on the thermal migration of charger carriers. Hereby, we measured the frequency-dependent impedance spectroscopy in the temperature range of 400–700 K for all the samples to explore the conductive behavior. Here we also take $x = 0.1$ as a typical example and the normalized impedance Z''/Z''_{max} for the sample $x = 0.1$ is given in Fig. 7(d). A well-defined Z''/Z''_{max} peak can be observed and this peak shifts to a higher frequency with increasing the temperature implying a typical thermal activated process of charge carriers [39]. The similar behavior can be observed for all the samples (not shown here). The activation energy from the well-defined Z''/Z''_{max} spectroscopy can be determined to be 0.73, 0.67, 0.80, and 0.73 eV for the samples with $x = 0$, 0.05, 0.1, and 0.15, respectively, as shown in the Fig. 7(f). Interestingly, we can find that the activation energies almost do not vary with x, implying the same charge carrier is responsible for the conductive behavior. At the same time, it can be noted that the Z''/Z''_{max} spectroscopy in high-frequency region has another one weak dielectric relaxation (as marked by the dotted line), which will be discussed in scaling behavior below.

In order to further elucidate which kind of charge carriers is responsible for the impedance relaxation and conductive behavior. The ac conductivity plots are also calculated based on the frequency dependence of the complex dielectric spectroscopy for all the samples. The ac conductivity can be fitted by Jonscher's power law for all the samples [40]. We take the sample with $x = 0$ and $x = 0.1$ as the typical examples to analyze the conductive behavior, as shown in Fig. 8 (a) and (b), respectively. The relationship between dc conductivity and temperature can be described by Arrhenius Law for all the samples, and the activation energy of dc conductivity can be determined to be 0.71, 0.68, 0.73, and 0.66 eV for the sample with $x = 0$, 0.05, 0.1, and 0.15, respectively, as shown in the inset of Fig. 8(b). Based on the activation energies derived from dc conductivity plots, we think the same charge carrier contributes to dc conductive behavior in all the samples. Meanwhile, we studied the dynamic process of charge carrier according to the scaling behavior of impedance Z'' at various temperature for the typical sample $x = 0.1$, as shown in Fig. 8 (c). A series of overlapped peaks can be observed illustrating the dynamic process of charge carrier is independence of temperature [41]. Certainly, the long-range migration or short-range hopping behavior of charge carrier is a very important reference to investigate the dielectric relaxation and dc conductive information in the samples. Hereby, we performed the normalized electric modulus M''/M''_{max} and impedance Z''/Z''_{max} at a certain temperature for all the samples, and these of the typical sample $x = 0.1$ at 450 K are displayed in Fig. 8(d). Both modulus M''/M''_{max} and impedance Z''/Z''_{max} have two relaxation peaks, as shown in Fig. 8 (d). The low-frequency Peak4 (P4) of M''/M''_{max} and Peak1 (P1) of Z''/Z''_{max} located at the same position indicating this kind of carrier shows a long-range movement behavior, which may be responsible for the dc conduction [34]. However, the high-frequency Peak3 (P3) of M''/M''_{max} and Peak4 (P4) of Z''/Z''_{max} shows an obvious separated behavior implying another kind of carrier exhibits a localized-hopping process, which may contribute to the dielectric relaxation [34,42].

Based on above results, we can note the activation energies of dielectric relaxation according to tanδ-T, tanδ-f, and M''-f spectra can be determined to be ~0.67 eV, ~0.50 eV, ~0.32 eV, and ~0.32 eV for the sample $x = 0$, 0.05, 0.1, and 0.15, respectively. However, the activation energies of Z''-f and dc conductivity are very close and ranging from 0.66 to 0.80 eV for all the samples. Therefore, we can
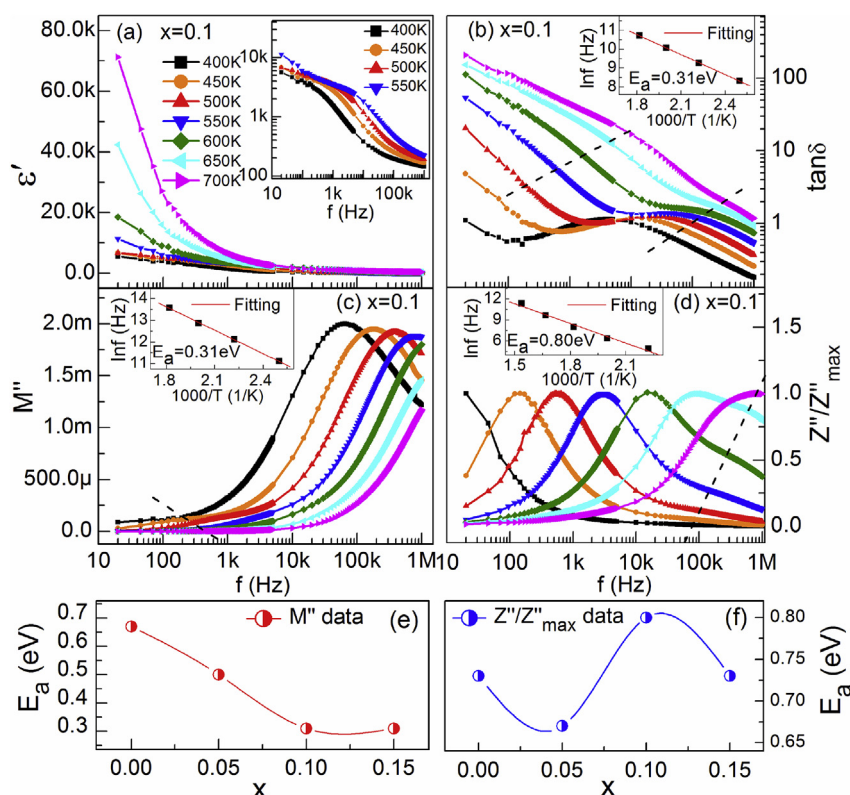
Fig. 7. (a) Frequency dependence of dielectric constant at different temperatures for sample $x = 0.1$, the inset of (a) shows the dielectric constant in logarithmic mode in the temperature from 400 K to 550 K. (b) Frequency dependence of dielectric loss for the sample $x = 0.1$, the inset of (b) shows the fitted result of dielectric loss relaxation at high frequency region. (c) Frequency dependence of electric modulus M'' spectroscopy at different temperatures for the sample $x = 0.1$, the inset of (c) shows the Arrhenius Law fitting result of relaxation. (d) Frequency dependence of the normalized impedance Z''/Z''_{max} at the different temperatures for the sample $x = 0.1$, the inset of (d) shows the fitted result of impedance relaxation. (e) The activation energies deduced from the electric modulus M'' relaxation for all the samples. (f) The activation energies deduced from the impedance Z'' relaxation for all the samples.

note the activation energies of dielectric relaxation and dc conductivity in sample $x = 0$ are very close whereas these of other three samples are different, which demonstrate that the dielectric relaxation and dc conductivity are associate with the same charge carrier in the sample $x = 0$ while the mechanism of dielectric relaxation is different from that of dc conductivity in other three samples. Nowadays, what types of carriers undertake the present dielectric relaxation and dc conductivity for each sample? On one hand, the values of 0.66–0.80 eV are comparable to that due to the long-rang migration of oxygen vacancies, such as: 0.59–0.78 eV in Bi:SrTiO$_3$ [43], 0.76 eV in Bi$_5$TiNbWO$_{15}$ [44], and 0.66 eV in Bi$_{4.2}$Nd$_{0.8}$Fe$_{0.5}$Co$_{0.5}$Ti$_3$O$_{15}$ [45]. The activation energies of 0.31 eV is in line with the localized hopping process of electrons, such as: 0.33 eV in Bi$_6$Fe$_2$Ti$_3$O$_{18}$ [34], 0.30 eV in Bi$_5$Fe$_{0.5}$Cr$_{0.5}$Ti$_3$O$_{15}$ [46], 0.38 eV in Sr(Fe$_{0.5}$Nd$_{0.5}$)O$_3$ [47], and 0.3 eV in BiFeO$_3$ [48]. On the other hand, the overlapped behavior of M''/M''_{max} and Z''/Z''_{max} peaks in the low-frequency region is ascribe to the long-rang migration of charge carrier whereas the separated behavior of M''/M''_{max} and Z''/Z''_{max} peaks in the high-frequency region is related to the localized movement process of charge carrier. Additionally, take into account of the mass of oxygen vacancies is much larger than that of electrons, and thus the movement of oxygen vacancies can only follow the change of bias electric field in low frequency region whereas the motion of electrons can quickly response to the variation of bias electric field in high frequency range. Thereby, the long-range migration of oxygen vacancies in low frequency region is responsible for dc conductivity and Z'' relaxation and the localized hopping process of electrons in high frequency range contributes to the M'' relaxation [43]. Based on the

above discussion, one dielectric relaxation observed in all the samples can be attributed to the long-range motion of oxygen vacancies, and another one dielectric relaxation in sample $x = 0.05$ can be attributed to the co-contribution of long-rang motion of oxygen vacancies and the localized hopping process of electrons, and that in the samples $x = 0.1$ and 0.15 may date from the localized hopping process of electrons. However, the dc conduction in all the samples can be ascribed to the long-range movement of oxygen vacancies.

It is well known that the presence of oxygen vacancies in Aurivillius ceramics is an inevitable fact. Hence, the oxygen vacancies exist in undoped sample BFTO. However, doping donor ions W^{6+} may introduce some electrons into sample, and a portion of electrons may compensate the oxygen vacancies existed in the samples, and the reminded electrons may be also thermal activated and give rise to the dielectric relaxation, as observed in the sample $x = 0.05$. With further increase the doping level x, the amount of electrons provided by donor ions W^{6+} will exceed the content of oxygen vacancies, and the excess electrons will mainly contribute to the dielectric relaxation, as evidence by the samples $x = 0.1$ and $x = 0.15$.

4. Conclusion

In summary, we have investigated the structural, magnetic, and dielectric properties of W/Cr co-doped Aurivillius Bi$_5$FeTi$_{3-3x}$(WCr$_2$)$_x$O$_{15}$ ($0 \leq x \leq 0.15$) ceramics. All the samples have an orthorhombic lattice with space group of $A2_1am$. The short-range AFM exchange interaction can be enhanced by co-doping W/Cr, and the
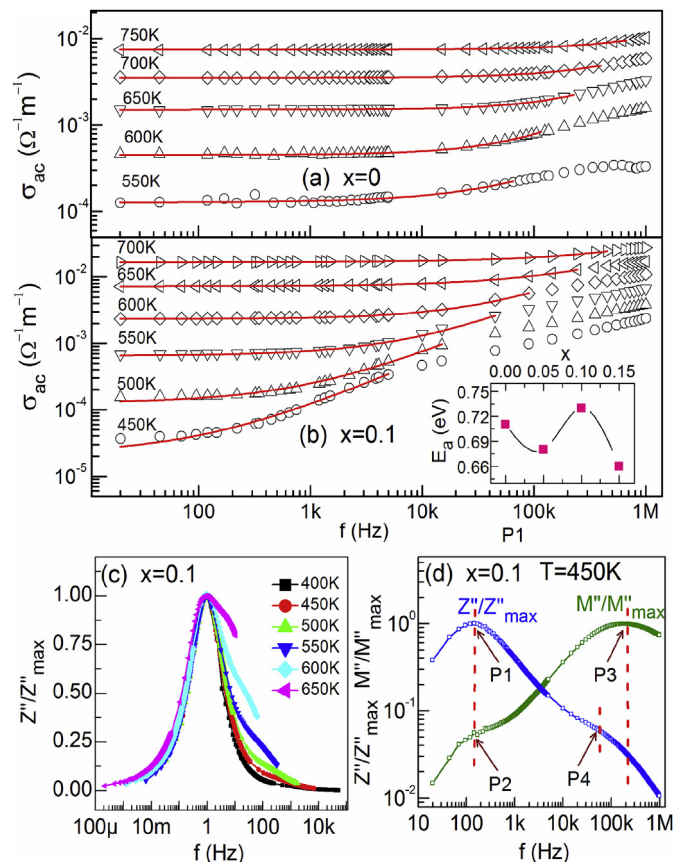
Fig. 8. Frequency dependence of *ac* conductivity σ_{ac} at various temperatures for the sample (a) $x = 0$ and (b) $x = 0.1$, respectively. The solid lines are the fitted results according to Jonscher's power law. The inset of (b) shows the activation energies deduced from *dc* conductivity for all the samples. (c) The scaling behavior of the normalized impedance Z''/Z''_{max} at various temperatures for the sample $x = 0.1$. (d) The normalized M''/M''_{max} and Z''/Z''_{max} at 450 K for the sample $x = 0.1$.

ferroelectric Curie temperature decreases from 1013 K to 965 K. The same dielectric relaxation induced by the thermal movement of oxygen vacancies can be observed in all the samples. However, another one dielectric relaxation can be only found in the doped samples, and this dielectric relaxation in sample $x = 0.05$ dates from the co-contribution of thermal movement of oxygen vacancies and electrons, and that in samples $x = 0.1$ and 0.15 stems from the localized hopping process of electrons. In addition, the *dc* conduction behavior in all the samples is originate from the long-range migration of oxygen vacancies.

Acknowledgement

References

[1] A. Imai, X. Cheng, H.L. Xin, E.A. Eliseev, A.N. Morozovska, S.V. Kalinin, R. Takahashi, M. Lippmaa, Y. Matsumoto, V. Nagarajan, ACS nano 7 (2013) 11079.
[2] A.Y. Birenbaum, C. Ederer, Phys. Rev. B 90 (2014) 214109.
[3] H.Y. Zhao, H. Kimura, Z.X. Cheng, M. Osada, J.L. Wang, X.L. Wang, S.X. Dou, Y. Liu, J.D. Yu, T. Matsumoto, T. Tohei, N. Shibata, Y. Ikuhara, Sci. Rep. 4 (2014) 5255.
[4] B. Aurivillius, Arki. Kemi 1 (1949) 463.
[5] B. Aurivillius, Arki. Kemi 1 (1949) 499.
[6] H.N. Lee, D. Hesse, N. Zakharov, U. Gosele, Science 296 (2002) 2006.
[7] S.E. Cummins, L.E. Cross, J. Appl. Phys. 39 (1968) 2268.
[8] Z.Y. Zhou, X.L. Dong, H. Chen, H.X. Yan, J. Am. Ceram. Soc. 89 (2006) 1756.
[9] G. Chen, W. Bai, L. Sun, J. Wu, Q. Ren, W.F. Xu, J. Yang, X.J. Meng, X.D. Tang, C.G. Duan, J.H. Chu, J. Appl. Phys. 113 (2013) 034901.
[10] X.Y. Mao, H. Sun, W. Wang, X.B. Chen, Y.L. Lu, Appl. Phys. Lett. 102 (2013) 072904.
[11] D.C. Meng, X.F. Zhai, C. Ma, H.L. Huang, Y. Yun, Y. Huang, Z.P. Fu, R.R. Peng, X.Y. Mao, X.B. Chen, G. Brown, Y.L. Lu, Appl. Phys. Lett. 106 (2015) 212906.
[12] J. Liu, W. Bai, J. Yang, Wenfei Xu, Y.Y. Zhang, T. Lin, X.J. Meng, C.G. Duan, X.D. Tang, J.H. Chu, J. Appl. Phys. 114 (2013) 234101.
[13] R.X. Ti, X.M. Lu, J. He, F.Z. Huang, H.R. Wu, F. Mei, M. Zhou, Y. Li, T.T. Xu, J.S. Zhu, J. Mater. Chem. C 3 (2015) 11868.
[14] L. Keeney, T. Maity, M. Schmidt, A. Amann, N. Deepak, N. Petkov, S. Roy, M.E. Pemble, R.W. Whatmore, J. Am. Ceram. Soc. 96 (2013) 2339.
[15] H.Y. Zhao, H. Kimura, Z.X. Cheng, M. Osada, J.L. Wang, X.L. Wang, S.X. Dou, Y. Liu, J.D. Yu, T. Matsumoto, T. Tohei, N. Shibata, Y. Ikuhara, Sci. Rep. 4 (2014) 5255.
[16] B. Yuan, J. Yang, J. Chen, X.Z. Zuo, L.H. Yin, X.W. Tang, X.B. Zhu, J.M. Dai, W.H. Song, Y.P. Sun, Appl. Phys. Lett. 104 (2014) 062413.
[17] S.F. Liu, Y.J. Wu, J. Li, X.M. Chen, Appl. Phys. Lett. 104 (2014) 082912.
[18] Gurvinderjit Singh, V.S. Tiwari, P.K. Gupta, J. Appl. Phys. 107 (2010) 064103.
[19] S. Zafar, R.E. Jones, B. Jiang, B. White, V. Kaushik, S. Gillespie, Appl. Phys. Lett. 73 (1998) 3533.
[20] J.F. Scott, C.A.P. Araujo, Science 246 (1989) 1400.
[21] Z.Y. Zhou, X.L. Dong, H. Chen, J. Am. Ceram. Soc. 89 (2006) 1756.
[22] Y. Chen, Z.H. Pen, Q.Y. Wang, J.G. Zhu, J. Alloys Compd. 612 (2014) 120.
[23] Z.Y. Zhou, Y.C. Li, S.P. Hui, X.L. Dong, Appl. Phys. Lett. 104 (2014) 012904.
[24] Z. Peng, Y. Chen, Q. Chen, N. Li, X. Zhao, C. Kou, D. Xiao, J. Zhu, J. Alloys Compd. 590 (2014) 210.
[25] J.B. Li, Y.P. Huang, G.H. Rao, G.Y. Liu, J. Luo, J.R. Chen, J.K. Liang, Appl. Phys. Lett. 96 (2010) 222903.
[26] J.G. Hou, Y.F. Qu, R. Vaish, K.B.R. Varma, D. Krsmanovic, R.V. Kumar, J. Am. Ceram. Soc. 93 (2010) 1414.
[27] R. Ramesh, N.A. Spaldin, Nat. Mater. 6 (2007) 21.
[28] D.L. Zhang, L. Feng, W.C. Huang, W.B. Zhao, Z.W. Chen, X.G. Li, J. Appl. Phys. 120 (2016) 154105.
[29] A. Punnoose, J. Hays, A. Thurber, M.H. Engelhard, R.K. Kukkadapu, C. Wang, V. Shutthanandan, S. Thevuthasan, Phys. Rev. B 72 (2005) 054402.
[30] H.X. Liu, B.B. Cao, C. O'Connor, J. Appl. Phys. 109 (2011) 07B516.
[31] C. Chen, K. Song, W. Bai, J. Yang, Y.Y. Zhang, P.H. Xiang, M.Y. Qin, X.D. Tang, J.H. Chu, J. Appl. Phys. 120 (2016) 214104.
[32] Y.Y. Liu, X.M. Chen, X.Q. Liu, L. Li, Appl. Phys. Lett. 90 (2007) 192905.
[33] S. Hunpratub, P. Thongbai, T. Yamwong, R. Yimnirun, S. Maensiri, Appl. Phys. Lett. 94 (2009) 062904.
[34] W. Bai, G. Chen, J.Y. Zhu, J. Yang, T. Lin, X.J. Meng, X.D. Tang, C.G. Duan, J.H. Chu, Appl. Phys. Lett. 100 (2012) 082902.
[35] A. Dutta, T.P. Sinha, J. Phys. Chem. Solids 67 (2006) 1484.
[36] V. Gupta, A. Mansingh, Phys. Rev. B 49 (1994) 1989.
[37] A. Srivastava, A. Garg, M.D. Morrison, J. Appl. Phys. 105 (2009) 054103.
[38] R.J. Tang, C. Jiang, J. Jian, Y. Liang, X. Zhang, H.Y. Wang, H. Yang, Appl. Phys. Lett. 106 (2015) 022902.
[39] M.F. Zhang, Y. Wang, K.F. Wang, J.S. Zhu, J.M. Liu, J. Appl. Phys. 105 (2009) 061639.
[40] A.K. Jonscher, Nature 267 (1977) 673.
[41] Q.Q. Ke, X.J. Lou, Y. Wang, J. Wang, Phys. Rev. B 82 (2010) 024102.
[42] D.K. Pradhan, N.P. Choudhary, C. Rinaldi, R.S. Katiyar, J. Appl. Phys. 106 (2009) 024102.
[43] C. Ang, Z. Yu, L.E. Cross, Phys. Rev. B 62 (2000) 228.
[44] W. Wang, X.J. Wang, J. Zhu, X.Y. Mao, X.B. Chen, Chin. Phys. Lett. 26 (2009) 047701.
[45] J. Yang, L.H. Yin, D.F. Shao, X.B. Zhu, J.M. Dai, Y.P. Sun, Europhys. Lett. 96 (2011) 67006.
[46] W. Bai, C. Chen, J. Yang, Y.Y. Zhang, R.J. Qi, R. Huang, X.D. Tang, C.G. Duan, J.H. Chu, Sci. Rep. 5 (2015) 17846.
[47] Y.Y. Liu, X.M. Chen, X.Q. Liu, L. Li, Appl. Phys. Lett. 90 (2007) 192905.
[48] S. Hunpratub, P. Thongbai, T. Yamwong, R. Yimnirun, S. Maensiri, Appl. Phys. Lett. 94 (2009) 062904.